

RESEARCH

Open Access



N^ε-carboxyethyl-lysine influences atherosclerotic plaque stability through ZKSCAN3 acetylation-regulated macrophage autophagy via the RAGE/LKB1/AMPK1/SIRT1 pathway

Zhongwei Liu^{1,2,3,4,5,6,7}, Jing Liu^{1,2,4}, Xiqiang Wang^{1,2,4}, Yong Zhang^{1,2,4}, Yanpeng Ma^{1,2,4}, Gongchang Guan^{1,2,4}, Ya Yuwen^{1,2,4,5}, Ni He^{1,2,4,6}, Hanxiu Liu^{1,2,3,6}, Xingfeng Yu⁸, Sen Ma³, Junkui Wang^{1,2,4*}, Jin Zhang^{9*}, Ling Zhu^{1,2,4*} and Yulian Zhang^{10*}

Abstract

Atherosclerosis, a chronic inflammatory condition characterized by plaque formation, often leads to instability, particularly under Type 2 diabetes mellitus (T2DM) conditions, which exacerbate cardiovascular risks. However, the molecular mechanisms underlying this process remain incompletely understood. In this study, we investigated the correlation between acute coronary syndrome (ACS) and serum levels of N^ε-carboxyethyl-lysine (CEL), a prominent advanced glycation end product (AGE) elevated in T2DM, in a cohort of 225 patients with coronary artery disease. Using a murine model of atherosclerosis complicated by T2DM, we examined the effects of CEL on plaque stability and macrophage autophagy. Our findings revealed that elevated serum CEL levels are independently associated with increased ACS incidence. Metabolomic profiling identified CEL as a key AGE contributing to plaque instability in diabetic conditions. Mechanistically, CEL disrupted macrophage autophagy and plaque stability by perturbing the Receptor for Advanced Glycation End products (RAGE)/Liver Kinase B1 (LKB1)/AMP-activated Protein Kinase 1 (AMPK1)/Sirtuin 1 (SIRT1) signaling cascade. This pathway further regulated autophagic activity through SIRT1-mediated acetylation of Zinc Finger with KRAB and SCAN Domains 3 (ZKSCAN3). These findings highlight CEL's critical role in promoting plaque instability in T2DM by impairing key molecular pathways that regulate autophagy, offering potential therapeutic targets for managing atherosclerosis in diabetic patients.

*Correspondence:

Junkui Wang
junkuiwang@yeah.net
Jin Zhang
zj_so@163.com
Ling Zhu
lingzhu2360@163.com
Yulian Zhang
zhangyulian0307@126.com

Full list of author information is available at the end of the article



© The Author(s) 2025. **Open Access** This article is licensed under a Creative Commons Attribution-NonCommercial-NoDerivatives 4.0 International License, which permits any non-commercial use, sharing, distribution and reproduction in any medium or format, as long as you give appropriate credit to the original author(s) and the source, provide a link to the Creative Commons licence, and indicate if you modified the licensed material. You do not have permission under this licence to share adapted material derived from this article or parts of it. The images or other third party material in this article are included in the article's Creative Commons licence, unless indicated otherwise in a credit line to the material. If material is not included in the article's Creative Commons licence and your intended use is not permitted by statutory regulation or exceeds the permitted use, you will need to obtain permission directly from the copyright holder. To view a copy of this licence, visit <http://creativecommons.org/licenses/by-nc-nd/4.0/>.

Keywords Advanced glycation end products, N^ε-carboxyethyl-lysine, Atherosclerotic plaque vulnerability, Macrophage autophagy, Type 2 diabetes mellitus

Introduction

Atherosclerosis, a progressive inflammatory disease, is characterized by the accumulation of lipids and fibrous elements in the arterial walls, leading to plaque formation, arterial narrowing, and potential cardiovascular events [1]. This pathological process is exacerbated in the presence of type 2 diabetes mellitus (T2DM), a metabolic disorder marked by insulin resistance and hyperglycemia. Cardiovascular disease, primarily driven by atherosclerosis, is a leading cause of morbidity and mortality among individuals with T2DM [2]. The intricate relationship between atherosclerosis and T2DM is multifaceted. For instance, accelerated progression of atherosclerosis making T2DM patients more susceptible to its complications [3]. Moreover, impaired glucose tolerance, a precursor to T2DM, has been independently associated with carotid atherosclerosis, further underscoring the intertwined nature of these conditions [4].

Macrophages, as integral components of the innate immune system, play a pivotal role in the pathogenesis of atherosclerosis, particularly in the context of plaque stability [5]. The functional heterogeneity of macrophages within the atherosclerotic plaque is noteworthy. Different macrophage phenotypes contribute variably to plaque progression and instability. Pro-inflammatory macrophages, for example, secrete matrix metalloproteinases (MMPs) and pro-inflammatory factors compromising the fibrous cap and rendering the plaque vulnerable to rupture [6]. Furthermore, the autophagy activity of macrophages, while essential for the clearance of apoptotic cells and debris, is critical for maintaining plaque stability. Impairment or exhaustion of macrophage autophagy leads to necrotic core expansion and increases the risk of plaque rupture [7].

Advanced Glycation End Products (AGEs) represent a diverse group of bioactive molecules formed through the non-enzymatic glycation of proteins, lipids, and nucleic acids. The formation and accumulation of AGEs are particularly pronounced under hyperglycemic conditions, making them highly relevant in the context of diabetes [8]. AGEs exert their pathophysiological effects primarily through interaction with their receptor, RAGE (Receptor for Advanced Glycation End Products). This interaction has been implicated in various inflammatory and oxidative stress pathways, contributing to the progression of numerous diabetic complications, including atherosclerosis [9]. The RAGE–AGE interaction amplifies the inflammatory response, fostering an environment conducive to atherosclerotic plaque formation and progression [10]. Moreover, AGEs have been associated with vascular

inflammation, a key player in the acceleration of atherosclerosis, especially in diabetic individuals [11].

N^ε-carboxyethyl-lysine (CEL) is one of the typical AGEs that has garnered attention in the context of diabetes and its associated complications, particularly atherosclerosis [12]. Upon formation, CEL can interact with specific receptors, notably the RAGE [13]. This interaction triggers a cascade of intracellular signaling events, leading to oxidative stress, inflammation, and endothelial dysfunction [14], all of which may be potentially involved in the pathogenesis of atherosclerosis. Furthermore, activation of RAGE has been shown to modulate various pathways related with cellular autophagy [15].

Given the association between macrophage autophagy and plaque stability, our hypothesis posits that in the diabetic environment, CEL may contribute to atherosclerotic plaque instability, potentially mediated through RAGE activation, which might indirectly influence the autophagy signaling pathways, leading to increased plaque vulnerability. In this study, metabolomics investigation was used to identify major AGEs including CEL, N^ε-carboxymethyl-lysine (CML), pentosidine, pyrroline and methylglyoxal-derived hydroimidazolone (MG-H1) in diabetic atherosclerotic animals. Effects of candidate AGEs on macrophage autophagy were also investigated. Furthermore, animal models were employed to assess the impact of CEL on plaque stability.

Materials and methods

Cohort study

Between May 2017 and May 2019, 240 patients diagnosed with coronary artery disease (CAD) affecting the left anterior descending artery (LAD) were initially recruited from Shaanxi Provincial People's Hospital. After applying exclusion criteria, the final cohort consisted of 225 participants. Exclusions were made for the following reasons: four patients had a diagnosis of malignant cancer; one patient had systemic lupus erythematosus; and ten patients developed acute heart failure requiring support with extracorporeal membrane oxygenation (ECMO) or left ventricular assist devices (LVADs). CAD and identification of the culprit vessel were confirmed via coronary angiography. Acute coronary syndrome (ACS) was diagnosed based on current guidelines [16]. T2DM was also diagnosed according to prevailing guidelines [17]. The exclusion criteria included: age under 18 or over 80 years; pregnancy; history of myocardial infarction; prior percutaneous coronary intervention or coronary artery bypass grafting (PCI/CABG); New York Heart Association (NYHA) functional class III or IV heart failure; renal

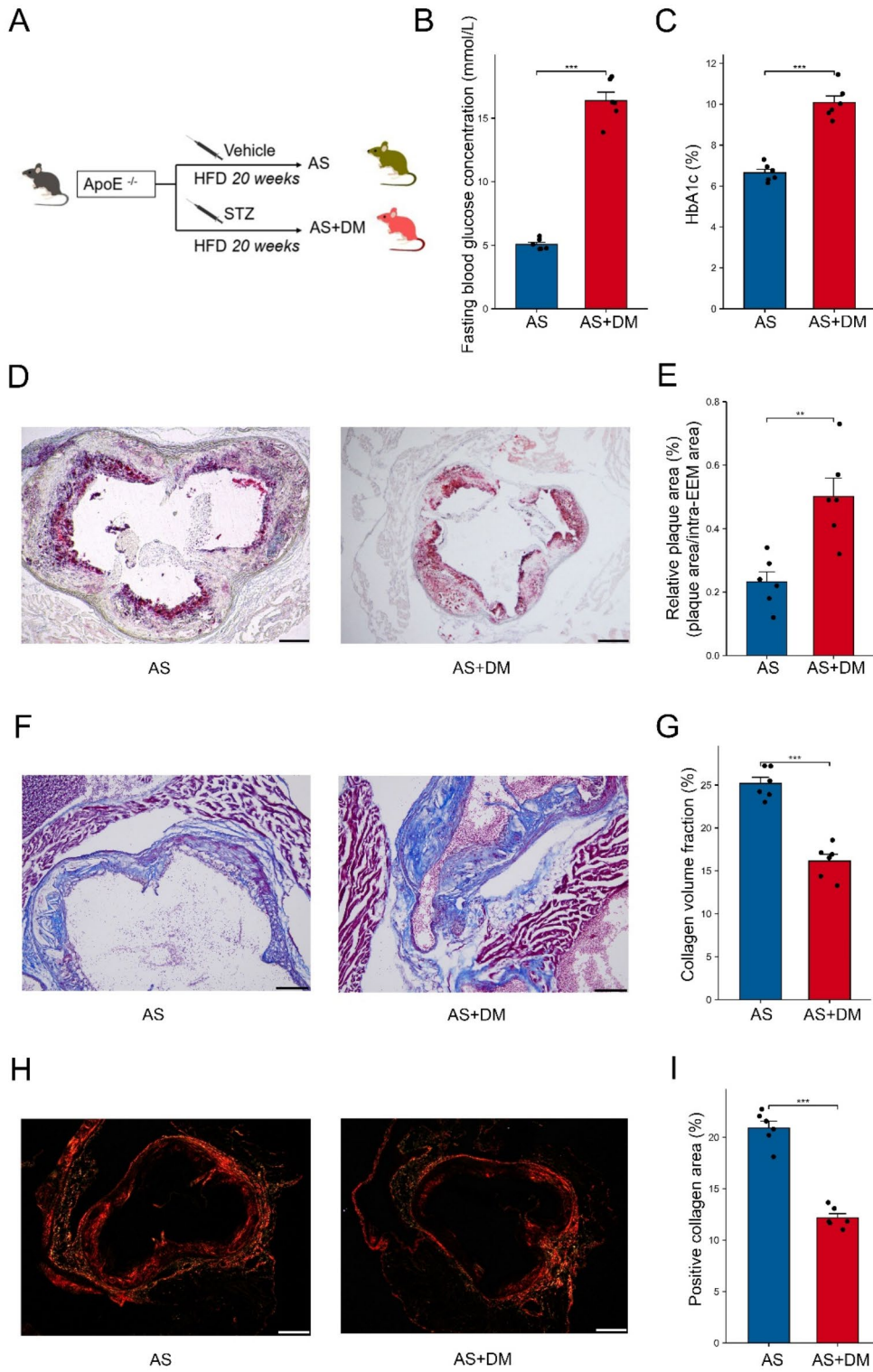


Fig. 1 (See legend on next page.)

(See figure on previous page.)

Fig. 1 Assessment of diabetes-exacerbated atherosclerosis in *ApoE*^{-/-} mice. Eight-week-old male C57BL/6J *ApoE*^{-/-} mice, some of which received streptozotocin (STZ) injections, were maintained on a high-fat diet (HFD) for 20 weeks to develop models of atherosclerosis (AS) and diabetes-aggravated atherosclerosis (AS+DM). **A**, Flowchart depicting the protocol for establishing the mouse models. **B**, Quantification of plasma fasting blood glucose concentrations in AS versus AS+DM mice. **C**, Measurement of plasma glycosylated haemoglobin (HbA1c) levels as a percentage in both groups. **D**, Oil Red O (ORO) staining of aortic root plaques to visualize lipid accumulation; scale bars, 200 μ m. **E**, Quantitative analysis of plaque area relative to the intra-external elastic membrane (EEM) area. **F**, Representative Masson's trichrome-stained sections of aortic root plaques, highlighting fibrous content; scale bar, 200 μ m. **G**, Collagen volume fraction in plaques measured in both models. **H**, Sirius Red staining of aortic plaques for collagen content visualization; scale bar, 200 μ m. **I**, Quantification of positive collagen area within plaques. Data represent mean \pm SD for $n=6$ mice per group; *** $P<0.001$, ** $P<0.01$, indicating significant differences between AS and AS+DM groups.

or hepatic dysfunction; malignant cancers; immune-mediated disorders; or mental health disorders. Peripheral venous blood samples were collected from fasting patients. The study protocol was approved by the ethics committee of the Shaanxi Provincial People's Hospital, and all participants provided informed consent for the use of their medical records and blood samples for research purposes.

Preparation and detection of CEL

CEL-BSA (Cell Biolabs) was used for in vitro experiments. For in vivo experiments, CEL was synthesized through a glycation reaction between sodium casein, a milk-derived protein, and lactose, a disaccharide carbohydrate. In the synthesis protocol, lactose was first solubilized in a 50 mmol/L sodium phosphate buffer (pH 8.5) to achieve a concentration of 0.25 mmol/L. Subsequently, sodium casein was introduced at a ratio of 1:7 (casein to lactose) and the mixture was subjected to a reaction at 140°C for a duration of 140 min. Post-reaction, the resultant mixture was concentrated using a vacuum rotary evaporator. To quantitatively assess CEL concentrations, high-performance liquid chromatography (HPLC) was performed using the 1260 Infinity II LC system equipped with a fluorescence detector (Agilent Technologies). The samples are prepared by adding 6% perchloric acid to precipitate proteins, followed by centrifugation to clear the supernatant. This supernatant is then derivatized with *o*-phthalaldehyde to enhance fluorescence detection of CEL. Analysis is conducted on a C18 column (250 mm x 4.6 mm, 5 μ m particle size; Agilent Technologies), using a mobile phase of acetonitrile and water (40:60 v/v) at a flow rate of 1.0 mL/min, and the fluorescence detector set to 230 nm for excitation and 450 nm for emission. CEL concentrations are determined by HPLC, comparing the sample's peak areas to those of a standard CEL calibration curve.

Establishment of animal models and treatments

At the onset of the study, 8-week-old *ApoE*^{-/-} mice (B6/JGpt-Apoeem1Cd82/Gpt, Strain NO.T001458, *ApoE*^{-/-} mice, GemPharmatech) were subjected to intraperitoneal injections of streptozotocin (STZ, Sigma-Aldrich) at a concentration of 50 mg/kg/day for a continuous span of five days. Post-treatment, mice exhibiting blood

glucose concentrations surpassing 300 mg/dL were delineated as diabetic. Following this classification, these mice were transitioned to a high-fat diet (HFD, D12079B, Research Diets Inc.) for a duration of 20 weeks (Fig. 1A). The specified diet derived its caloric distribution as 42% from fats (equivalent to 21 g/100 g of the diet, primarily sourced from lard), 43% from carbohydrates, and 15% from proteins, supplemented with 0.15% cholesterol. As demonstrated in Fig. 4A, several *ApoE*^{-/-} mice were administered with CEL orally at a dosage of 2 mg/kg/d for 20w alongside either a SIRT1 inhibitor EX527 or a SIRT1 agonist SRT1720. EX527 (Millipore Sigma) was administered at a dosage of 0.5 mg/kg/d, while SRT1720 (Millipore Sigma) was given at a dosage of 1 mg/kg/d orally for the same duration [18]. A one-week acclimatization phase was instituted to ensure optimal adaptation of the mice to the experimental conditions.

Metabolomics profiling

For metabolomics analysis, blood samples were meticulously procured from *ApoE*^{-/-} mice immediately upon euthanasia, ensuring a standardized approach to sample collection. The analytical framework employed liquid chromatography coupled with mass spectrometry (LC/MS) to scrutinize the metabolic extracts derived from a methanol-facilitated protein precipitation technique. Specifically, the Acquity I-Class PLUS ultra-high-performance liquid chromatograph (Waters) in tandem with the Xevo G2-XS QTOF high-resolution mass spectrometer (Waters) was utilized, incorporating an Acquity UPLC HSS T3 column (Waters). The chromatographic conditions were defined by a mobile phase consisting of a 0.1% formic acid in both water and acetonitrile, with a consistent injection volume set at 1 μ L. The Xevo G2-XS QTOF was adeptly calibrated to acquire both precursor and product ion spectra in MSe mode, governed by the MassLynx V4.2 software (Waters). This configuration permitted concurrent data acquisition at both low (set at 2 V) and gradient high collision energies (ranging from 10 to 40 V) within each analytical cycle. The instrument was set to a scan frequency of 0.2 s per spectrum. The ESI ion source parameters were meticulously adjusted to: capillary voltage of 2000 V (in positive ion mode) or -1500 V (in negative ion mode); cone voltage at 30 V; ion source temperature at 150 °C; desolvation gas temperature at

500 °C; backflush gas flow rate at 50 L/h; and a desolvation gas flow rate of 800 L/h. Raw data acquisition was facilitated by the MassLynx software (V4.2, Waters), post which the Progenesis QI software (V2.0, Waters) was employed for tasks such as peak extraction, alignment, and normalization. Compound elucidation was proficiently achieved using the integrated Progenesis QI software's METLIN database, complemented by a bespoke library (Biomark). This ensured that the theoretical fragment identification and mass deviation remained stringently within a 100ppm threshold. MassLynx software (V4.2, Waters) was used to capture raw data, which was then processed by Progenesis QI software (V2.0, Waters) for peak extraction, peak alignment, and other data operations. Compound identification was aided by the Progenesis QI software online METLIN database and a self-constructed library (Biomark), ensuring that the theoretical fragment identification and mass deviation were within the defined 100ppm limit.

Histology

Aortic root samples extracted from the mice were subjected to a comprehensive histological analysis. Initially, the specimens underwent fixation in a 10% neutral buffered formalin solution (Sigma-Aldrich). Following fixation, they were embedded in optimal cutting temperature (OCT) compound (Sakura Finetek). Aortic root sections, precisely sectioned to a thickness of 10 µm using a cryostat, were stained with Oil Red O (Sigma-Aldrich) to delineate lipid accumulation. Hematoxylin (Sigma-Aldrich) was employed as a counterstain, accentuating the nuclei. For the evaluation of collagen distribution, the aortic root sections were subjected to both Masson's Trichrome and Sirius Red staining procedures. In the Masson's Trichrome protocol, sections were sequentially exposed to Weigert's iron hematoxylin (Sigma-Aldrich), Biebrich scarlet-acid fuchsin (Sigma-Aldrich), phosphomolybdic-phosphotungstic acid (Sigma-Aldrich), and culminated with aniline blue (Sigma-Aldrich) application. The Sirius Red staining regimen encompassed an hour-long incubation in Sirius Red solution (comprising Direct Red 80 in saturated picric acid, Sigma-Aldrich), succeeded by a brief rinse in acidified water. Upon completion of the staining processes, sections were methodically dehydrated, cleared, and sealed with a mounting medium (Sigma-Aldrich). The meticulously stained sections were then examined under a light microscope, with representative images captured to facilitate subsequent quantitative assessments.

Immunofluorescent stains

Aortic root specimens were sectioned to a precise thickness of 10 µm after embedding in OCT compound (Sakura Finetek). Following sectioning, the samples

underwent permeabilization with a 0.3% Triton X-100 solution (Sigma-Aldrich) in phosphate-buffered saline (PBS) for a duration of 15 min. To minimize non-specific binding, sections were blocked using 5% (BSA, Sigma-Aldrich) in PBS and incubated for 1 h at ambient temperature. Subsequently, the sections were treated with primary antibodies: anti-F4/80 (1:200, Abcam) and anti-LC3B (1:200, Abcam), and incubated in a 4 °C environment overnight. Post-primary antibody incubation, sections were rinsed and exposed to secondary antibodies: Alexa Fluor 488-conjugated anti-rat IgG (1:500, Invitrogen) and Alexa Fluor 594-conjugated anti-rabbit IgG (1:500, Invitrogen), with an incubation period of 1 h at room temperature. Following secondary antibody application, sections were washed and mounted using Vectashield Antifade Mounting Medium integrated with DAPI (Vector Laboratories) to accentuate the nuclei. Fluorescent imaging was conducted using a confocal microscope (Leica Microsystems), with subsequent analysis focusing on the colocalization and expression dynamics of the proteins of interest.

Macrophages and treatments

Primary mice peritoneal macrophages were isolated through peritoneal lavage. Mice received an intraperitoneal injection of 3 ml sterile 3% Brewer thioglycolate medium (Sigma-Aldrich). Four days subsequent to the injection, mice were euthanized, and the peritoneal cavity was lavaged with 8 ml of ice-cold phosphate-buffered saline (PBS, Gibco). The retrieved peritoneal exudates were subjected to centrifugation at 300xg for 5 min. The resultant cell pellet was resuspended in Dulbecco's Modified Eagle Medium (DMEM, Gibco) fortified with 10% fetal bovine serum (FBS, Gibco), 100 U/ml penicillin, and 100 µg/ml streptomycin (Gibco). Cells were then allocated to tissue culture plates and incubated at 37 °C in a 5% CO₂ atmosphere for 2 h to facilitate macrophage adherence. Post-incubation, non-adherent cells were meticulously discarded, leaving behind a monolayer of adherent macrophages ready for subsequent experimental procedures. THP-1 cells were obtained from ATCC and cultured in DMEM medium supplemented with 10% FBS. CEL was dissolved in DMSO and added to cell culture media at final concentrations of 0, 125, 250, 500, 750, 1000, 1250, and 1500 µg/L. Mouse primary macrophages and THP-1 cells were treated with CEL for 48 h before further analyses. Several macrophages were pre-treated with EX527 (10 µmol/L) and/or SIRT1720 (1 µmol/L) for 24 h, as supported by previous studies demonstrating effective modulation of SIRT1 activity within this time-frame [19–21]. To ensure the selected concentrations were appropriate, a concentration-response analysis was performed, and the results are provided in Fig. S1.

Cell viability assay

Cell viability was determined using the Cell Counting Kit-8 (CCK-8, Beyotime). Mouse primary macrophages and human THP-1 cells were seeded in 96-well plates at a density of 1×10^4 cells per well. After treatment, 10 μ L of CCK-8 solution was added to each well and the plates were incubated at 37 °C for 2 h. The absorbance was measured at 450 nm using a microplate reader (BioTek). Relative cell viability was calculated using the following formula: cell viability (%) = $OD_{\text{treated}}/OD_{\text{control}} \times 100$. The results, presented in Fig. S2, demonstrate the dose-dependent effects of CEL and indicate that concentrations below 1000 μ g/L preserve cell viability while modulating SIRT1 activity.

Gene silencing and overexpression

To evaluate the role of RAGE, LKB1, and AMPK1 in CEL-mediated effects, genetic manipulation was performed in mouse macrophages. RAGE knockdown was achieved using specific siRNA (Santa Cruz), while LKB1 and AMPK1 were overexpressed using plasmids (Addgene). Scrambled siRNA (Santa Cruz) was used as a negative control. Lipofectamine reagents (Thermo Fisher) were used for transfections, following manufacturer protocols. Cells were incubated for 48 h for gene silencing or overexpression. Efficiency was confirmed via qRT-PCR and Western blotting, showing significant changes in mRNA and protein levels. Macrophages were divided into experimental groups, including control, CEL treatment, RAGE knockdown, LKB1 overexpression, AMPK1 overexpression, and combinations thereof. CEL treatment was administered at a concentration of 250 μ g/L for 48 h following genetic manipulation to assess its effects under different conditions.

Transmission electron microscopy (TEM) autophagy detection

Cultured macrophages were fixed in 2.5% glutaraldehyde (Sigma-Aldrich) prepared in 0.1mmol/L cacodylate buffer for 1 h at room temperature. After three washes in 0.1mmol/L cacodylate buffer, cells underwent a 1-hour post-fixation in 1% osmium tetroxide (Sigma-Aldrich). Subsequent staining was performed with 2% uranyl acetate (Sigma-Aldrich) for 30 min in the dark. Dehydration was achieved through sequential 10-minute immersions in increasing ethanol concentrations (50%, 70%, 90%, and 100%) followed by two 10-minute incubations in propylene oxide (Sigma-Aldrich). Cells were then embedded in epoxy resin (Sigma-Aldrich) and allowed to polymerize at 60 °C for 48 h. Sections of 60–90 nm thickness were generated using an ultramicrotome (Leica Microsystems) and collected on copper grids. For enhanced contrast, sections were treated with lead citrate (Sigma-Aldrich) for 5 min, then visualized under a transmission electron

microscope (Leica Microsystems) to identify and quantify characteristic autophagic structures.

Autophagic flux assessment

Macrophages were transduced with the mCherry-GFP-LC3B fusion protein using the Ad-mCherry-GFP-LC3B recombinant adenovirus (Beyotime) at a multiplicity of infection (MOI) of 20. After a 24-hour incubation period, cells were subjected to CEL, EX527 and SIRT1720 treatments. Fluorescence microscopy (Leica Microsystems) was then employed to visualize the mCherry (red) and GFP (green) fluorescence signals. The emergence of yellow puncta (co-localization of red and green signals) indicated the presence of autophagosomes, while isolated red puncta were indicative of autolysosomes. In this study, we employed a dual approach to assess autophagic flux by counting yellow puncta and measuring the ratio of mCherry to GFP fluorescence intensity.

Quantitative real-time PCR (qRT-PCR)

Total RNA was meticulously extracted from cultured macrophages employing the RNeasy Mini Kit (Qiagen), adhering strictly to the manufacturer's protocol. RNA integrity and concentration were ascertained using a NanoDrop spectrophotometer (Thermo Fisher Scientific). From the isolated RNA, 1 μ g was reverse transcribed to cDNA utilizing the High-Capacity cDNA Reverse Transcription Kit (Applied Biosystems). Quantitative real-time PCR assays were executed using the PowerUp SYBR Green Master Mix (Applied Biosystems) and conducted on the QuantStudio 5 Real-Time PCR System (Thermo Fisher Scientific). Primers specific for both mice and human *rage*, *sirt1*, and the housekeeping gene *actin* were employed, with sequences detailed in Table S1. Amplification parameters were set as follows: an initial 95 °C for 10 min, succeeded by 40 cycles of 95 °C for 15 s and 60 °C for 1 min. Expression quantification of the target genes was achieved using the $2^{-\Delta\Delta C_t}$ method, with GAPDH serving as the normalization control.

Immunoprecipitation and Western blots

To evaluate the acetylation status of Zinc Finger with KRAB and SCAN Domains 3 (ZKSCAN3), an immunoprecipitation protocol was adopted. Cell lysates were generated using a lysis buffer fortified with protease and phosphatase inhibitors. The BCA protein assay was employed to assess protein concentrations. Equal protein aliquots (500 μ g) underwent pre-clearance with protein A/G agarose beads (Santa Cruz Biotechnology) for 1 h at 4 °C. Subsequently, the pre-cleared lysates were incubated overnight at 4 °C with an anti-ZKSCAN3 antibody (1:1000, Abcam). Protein A/G agarose beads were introduced to the mixture for an additional 2-hour incubation at 4 °C. Following three washes with lysis buffer,

the proteins bound to the beads were eluted by boiling in 2×Laemmli sample buffer. For the western blot procedure, the eluted proteins and total cell lysates intended for RAGE, SIRT1, LKB1, and AMPK evaluations were resolved on 10–12% SDS-PAGE gels and subsequently transferred onto PVDF membranes (Millipore). Membranes were blocked using 5% non-fat milk in TBST for 1 h at room temperature. They were then incubated overnight at 4 °C with primary antibodies: anti-ZKSCAN3 (1:1000, Abcam), anti-acetylated lysine (1:1000, Cell Signaling Technology), anti-RAGE (1:800, Sigma-Aldrich), anti-SIRT1 (1:1000, Cell Signaling Technology), anti-phospho-LKB1 (1:1000, Cell Signaling Technology), and anti-phospho-AMPK (1:1000, Cell Signaling Technology). Post-primary antibody incubation, membranes were washed and exposed to horseradish peroxidase-conjugated secondary antibodies (1:5000, Abcam) for 1 h at room temperature. Visualization of protein bands was achieved using an enhanced chemiluminescence detection system (Thermo Fisher Scientific), and densitometric analysis facilitated the quantification of relative protein expression and phosphorylation levels.

Chromatin immunoprecipitation (ChIP)

To determine the binding affinity of ZKSCAN3 to the *map1lc3b* promoter, a ChIP assay was performed. Cells were cross-linked using 1% formaldehyde for 10 min at room temperature, ensuring the preservation of protein-DNA interactions. This reaction was terminated using 0.125 M glycine. Following cell lysis, chromatin was sheared into fragments of approximately 200–500 bp

through sonication. The sheared chromatin, amounting to 500 µg, underwent a pre-clearance step with protein A/G agarose beads (Santa Cruz Biotechnology) to diminish non-specific interactions. From this, 50 µg was reserved as an input control. The remaining 450 µg of chromatin was incubated with 5 µg of anti-ZKSCAN3 antibody (Abcam) overnight at 4 °C. To capture the antibody-chromatin complexes, protein A/G agarose beads were added and the mixture was incubated for an additional 2 h. After thorough washing to remove unbound chromatin, the protein-DNA complexes were decross-linked by heating at 65 °C overnight. The DNA was then extracted, purified, and subjected to PCR using primers specific for the *map1lc3b* promoter region (Table S2). The amplified products were visualized on agarose gels to confirm the specific binding of ZKSCAN3 to the *map1lc3b* promoter.

SIRT1 activity and NAD⁺ level assay

The catalytic activity of SIRT1 and NAD⁺ level were detected by using a SIRT1 Activity Assay kit (Abcam) and NAD/NADH Assay kit (Abcam) in macrophage cell lysates respectively. The detection protocols were carried out by following the instruction of the manufacturer.

Statistics

All data are represented as the mean ± standard deviation (SD), unless stated otherwise. The Shapiro-Wilk test was applied to confirm the normality of data distribution. For pairwise comparisons, the Student's t-test was utilized. In instances where multiple groups were compared, a one-way analysis of variance (ANOVA) was conducted, followed by a post hoc Tukey's test. Pearson's correlation analysis was employed to determine linear relationships between variables. The association between serum CEL and ACS was estimated with univariate and multivariate logistic regression models. All statistical testing was two-sided. A P-value less than 0.05 was deemed statistically significant. All statistical evaluations were executed using SPSS software (version 26.0, IBM Statistics).

Results

Serum CEL concentration elevation in T2DM was correlated with ACS

Data were successfully collected from 225 patients diagnosed with CAD. The baseline characteristics are summarized in Table 1, where patients were categorized into T2DM and non-T2DM groups. The T2DM group exhibited significantly higher fasting blood glucose levels, serum HbA1c concentrations, and incidence of ACS compared to the non-T2DM group. To explore the relationship between ACS and serum free CEL concentrations, both univariate and multivariate logistic regression analyses were conducted. As shown in Table 2, the

Table 1 Baseline characteristics of the patients with T2DM and Non-T2DM

Characteristics	Non-T2DM (n=150)	T2DM (n=75)	P value
Age (years)	54.86 ± 3.84	53.45 ± 4.39	0.014
Male (%)	92 (61.3)	45 (60)	0.847
BMI (kg/m ²)	24.18 ± 1.58	24.11 ± 1.47	0.745
Smoking (%)	48 (32)	39 (52)	0.004
Fasting blood glucose (mmol/L)	5.57 ± 0.72	12.24 ± 3.79	< 0.001
HbA1c (%)	5.1 ± 0.73	7.88 ± 1.58	< 0.001
ALT (U/L)	27.28 ± 7.8	26.62 ± 7.29	0.545
AST (U/L)	50.15 ± 29.08	51.48 ± 30.83	0.752
Triglyceride (mmol/L)	1.38 ± 0.44	1.25 ± 0.49	0.053
Total cholesterol (mmol/L)	3.51 ± 0.59	3.49 ± 0.64	0.827
LDL-cholesterol (mmol/L)	2.04 ± 0.67	1.91 ± 0.71	0.198
Troponin I (µg/L)	2.34 ± 3.26	2.59 ± 3.81	0.610
BNP (ng/L)	62.16 ± 22.21	65.37 ± 19.69	0.289
Free CEL (nmol/L)	48.04 ± 10.67	62.16 ± 10.67	< 0.001
ACS (%)	34 (22.67)	37 (49.33)	< 0.001

BMI, body mass index; ALT, alanine aminotransferase; AST, glutamic oxalacetic transaminase; LDL, low-density lipoprotein; BNP, B-type natriuretic peptide; ACS, acute coronary syndrome; Values are percent or means ± SD

univariate Cox regression model (Model 1) revealed that higher serum free CEL concentrations were significantly associated with the presence of ACS, with an odds ratio (OR) of 2.44 (95% confidence interval [CI]: 1.36–4.38, $P=0.003$). Further multivariate analysis adjusted for age and sex (Model 2) confirmed that serum free CEL concentration independently predicted ACS occurrence (adjusted OR=2.32, 95% CI: 1.23–4.05, $P=0.008$). The association remained robust in Model 3, which additionally adjusted for age, sex, body mass index, cigarette smoking, serum low-density lipoprotein levels, serum creatinine levels, and serum uric acid levels, yielding an adjusted OR of 3.06 (95% CI: 1.55–6.04, $P=0.001$).

Plaque instability is augmented in atherosclerotic mice with T2DM

In our murine model, atherosclerosis complicated with T2DM manifested heightened plaque instability. The successful induction of diabetes in the model was validated by a marked elevation in both fasting blood glucose and glycosylated hemoglobin A1c (HbA1c) levels (Fig. 1B–C). Atherosclerotic plaque formation was evident in both the atherosclerotic (AS) and the atherosclerotic with T2DM (AS+DM) animals, as delineated by Oil Red O (ORO) staining. Notably, the AS+DM group exhibited a pronounced plaque burden compared to their AS counterparts (Fig. 1D–E). Further histological assessments using Masson's trichrome and Sirius red stains (Fig. 1F–G and H–I) revealed a significant diminution in plaque collagen content within the AS+DM group, underscoring the heightened vulnerability of these plaques.

Distinct metabolic signatures in atherosclerotic mice with T2DM were revealed by metabolomic profiling

To ensure the precision and reliability of our metabolomic data, rigorous quality control (QC) was implemented, with Pearson correlation analysis validating the consistency and dependability of the results. Both negative and positive electrospray ionization modes (ESI- and ESI+, respectively) consistently exhibited a high Pearson correlation, underscoring the reproducibility and robustness of our analytical approach (Figure S3). The simultaneous use of ESI+ and ESI- ionization modes is critical for comprehensive metabolic profiling, as each mode offers complementary coverage of metabolite classes. Annotation identified 2,125 metabolites in ESI+ and 5,899 in ESI-. Distinct metabolic profiles between AS+DM

and AS mice were evident in orthogonal partial least squares discriminant analysis (OPLS-DA) score plots for both ESI+ (Fig. 2A) and ESI- modes (Figure S4A). Validation metrics, R² and Q², reinforced the credibility of the OPLS-DA models in ESI+ (Fig. 3B) and ESI- (Figure S4B), ensuring both model fit and predictive accuracy. Differential metabolites between AS+DM and AS groups were highlighted in volcano plots for both ESI+ (Fig. 2C) and ESI- modes (Figure S4C). Pathway analysis using the HMDB revealed that the altered metabolites were primarily enriched in carboxylic acids and derivatives, fatty acyls, and prenol lipids. These categories indicate disruptions in lipid metabolism, which are closely linked to atherosclerosis progression. Similarly, KEGG pathway enrichment analysis showed significant enrichment in tyrosine metabolism and biosynthesis of unsaturated fatty acids. These pathways highlight the interplay between amino acid metabolism, lipid biosynthesis, and inflammatory responses in the context of T2DM-associated atherosclerosis. Among the significantly altered AGEs, CEL and pyrrolidine were identified, whereas other AGEs such as CML, pentosidine, and MG-H1 were not detected. (Fig. 2F).

Serum CEL was associated with plaque vulnerability and macrophage autophagy in atherosclerotic mice complicated with T2DM

In our murine model of atherosclerosis with T2DM, we delineated the interrelationships between serum CEL concentrations, atherosclerotic plaque stability, and macrophage autophagy within the plaques. Serum concentrations of CEL and pyrrolidine in AS and AS+DM mice are depicted in Fig. 3A and B. Notably, the AS+DM group exhibited a pronounced elevation in serum CEL levels compared to the AS group, whereas the rise in serum pyrrolidine was not statistically significant between the two cohorts. Pearson's correlation analysis, as presented in Fig. 3C and D, revealed a significant inverse relationship between serum CEL concentrations and both the collagen volume fraction (as indicated by Masson's trichrome stain) and the positive collagen area (as determined by Sirius red stain), suggesting an inverse association between CEL levels and plaque stability. Immunofluorescence staining, showcased in Fig. 3E and F, revealed a discernible co-localization of F4/80 and LC3B within the atherosclerotic plaques of both AS and AS+DM mice. A reduction in autophagic activity, as suggested

Table 2 Univariate and multivariate logistic analysis as a continuous variable of serum CEL concentration

	Model 1*		Model 2†		Model 3‡	
	OR (95% CI)	p Value	OR (95% CI)	p Value	OR (95% CI)	p Value
CAD (n=225)	2.44 (1.36–4.38)	0.003	2.32 (1.23–4.45)	0.008	3.06 (1.55–6.04)	0.001

BMI, body mass index; LDL, low-density lipoprotein; UA, Uric Acid. Model 1 indicates the univariate regression analysis; Model 2 is adjusted for age and sex; Model 3 is further adjusted for age, sex, BMI, LDL, cigarette smoking, serum creatinine and UA

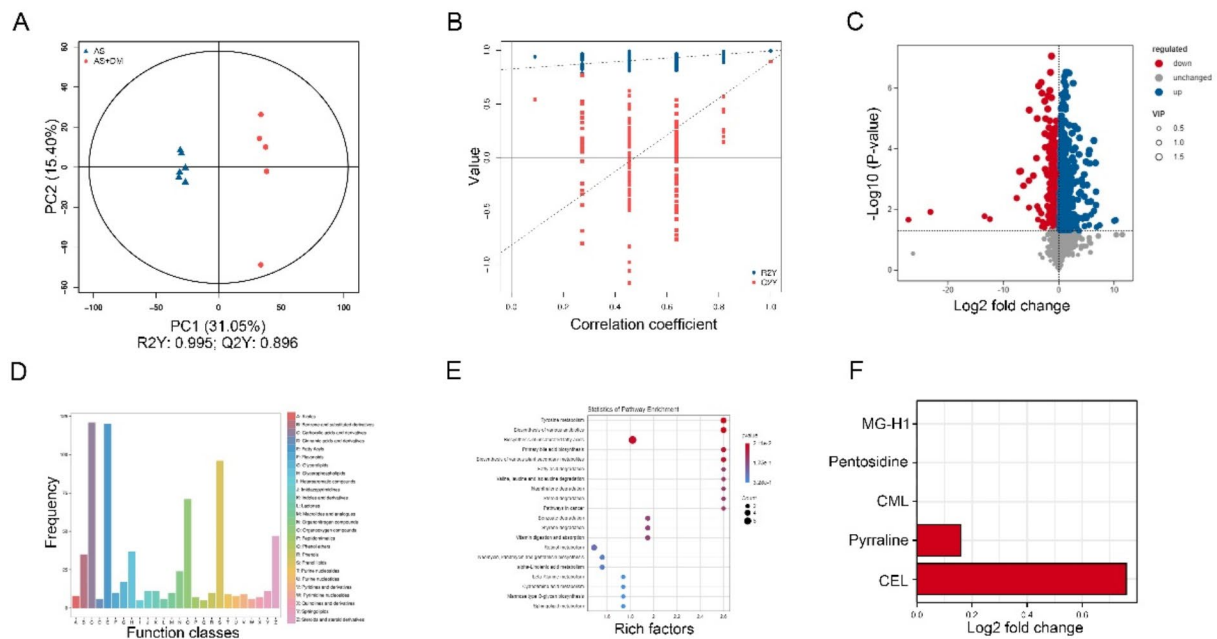


Fig. 2 Differential metabolomic profiling of mice model of atherosclerosis complicated with diabetes. **A**, Orthogonal partial least squares discriminant analysis (OPLS-DA) scatter plot displaying the metabolomic profiles of serum samples from AS (blue) and AS+DM (red) mice in positive electrospray ionization mode (ESI+). The axes represent the contributions of individual samples to the first two principal components (PC1 and PC2). **B**, Cross-validation plot for the OPLS-DA model with 200 permutations, demonstrating the model's validity through intercepts $R^2=(0.0, 0.995)$ and $Q^2=(0.0, 0.896)$, which indicate robustness and an absence of overfitting. **C**, Volcano plot showing pairwise metabolite comparisons between AS+DM and AS mice. Vertical dashed lines represent a twofold change threshold, and the horizontal dashed line indicates the $P=0.05$ significance level. Metabolites with significant changes are highlighted: up-regulated in blue and down-regulated in red. **D** and **E**, Metabolomic profiling annotated by the Human Metabolome Database (HMDB) and Kyoto Encyclopedia of Genes and Genomes (KEGG), respectively, elucidates significant metabolic alterations in AS+DM compared to AS under ESI+ conditions. **F**, Differential levels of advanced glycation end-products (AGEs), including carboxymethyl-lysine (CML), carboxyethyl-lysine (CEL), pyrraline, pentosidine, and methylglyoxal-derived hydroimidazolone (MG-H1), in AS+DM versus AS mice

by decreased colocalization of LC3B with macrophages, was observed in the plaques of AS+DM mice compared to the AS group. Further, Pearson's correlation analysis, as illustrated in Fig. 4G, established a significant negative correlation between serum CEL levels and macrophage autophagic activity within the plaques. Additionally, as evidenced in Fig. 3H and I, macrophage autophagic activity within the plaques exhibited a significant inverse correlation with both the collagen volume fraction and the positive collagen area, reinforcing the notion that reduced macrophage autophagic activity is associated with compromised plaque stability.

CEL exposure exacerbated atherosclerotic plaque vulnerability via suppressing macrophage autophagy

In our investigations, as depicted in Fig. 4B–C, AS mice exposed to CEL exhibited a pronounced plaque burden compared to their non-exposed counterparts. Notably, neither EX527 nor SRT1720 treatments significantly altered the plaque burden in CEL-administered AS mice. EX527, a selective SIRT1 inhibitor, and SRT1720, a potent SIRT1 agonist, were utilized to explore the role of SIRT1 in the regulation of macrophage autophagy and

plaque stability. These compounds allowed us to modulate SIRT1 activity pharmacologically and investigate its contribution to the effects of CEL on macrophage function and atherosclerotic plaques. Detailed histological analyses, presented in Fig. 4D and G, revealed that SRT1720 treatment led to a marked preservation in plaque collagen volume fraction (as indicated by Masson's trichrome stain) and the positive collagen area (as evidenced by Sirius red stain), which was impaired by co-treatment of EX527. Further, immunofluorescence analyses, showcased in Fig. 4H and K and Figure S5, indicated that SRT1720 treatment substantially preserved macrophage autophagic activity within the plaques, as evidenced by LC3B staining. TEM provided additional evidence, demonstrating that CEL treatment significantly reduced the number of autophagosomes in macrophages, which was effectively reversed by SRT1720 treatment. Conversely, co-treatment of EX527 effectively impaired SRT1720's retaining ability on macrophage autophagic activity in the atherosclerotic plaques of CEL-exposed AS mice.

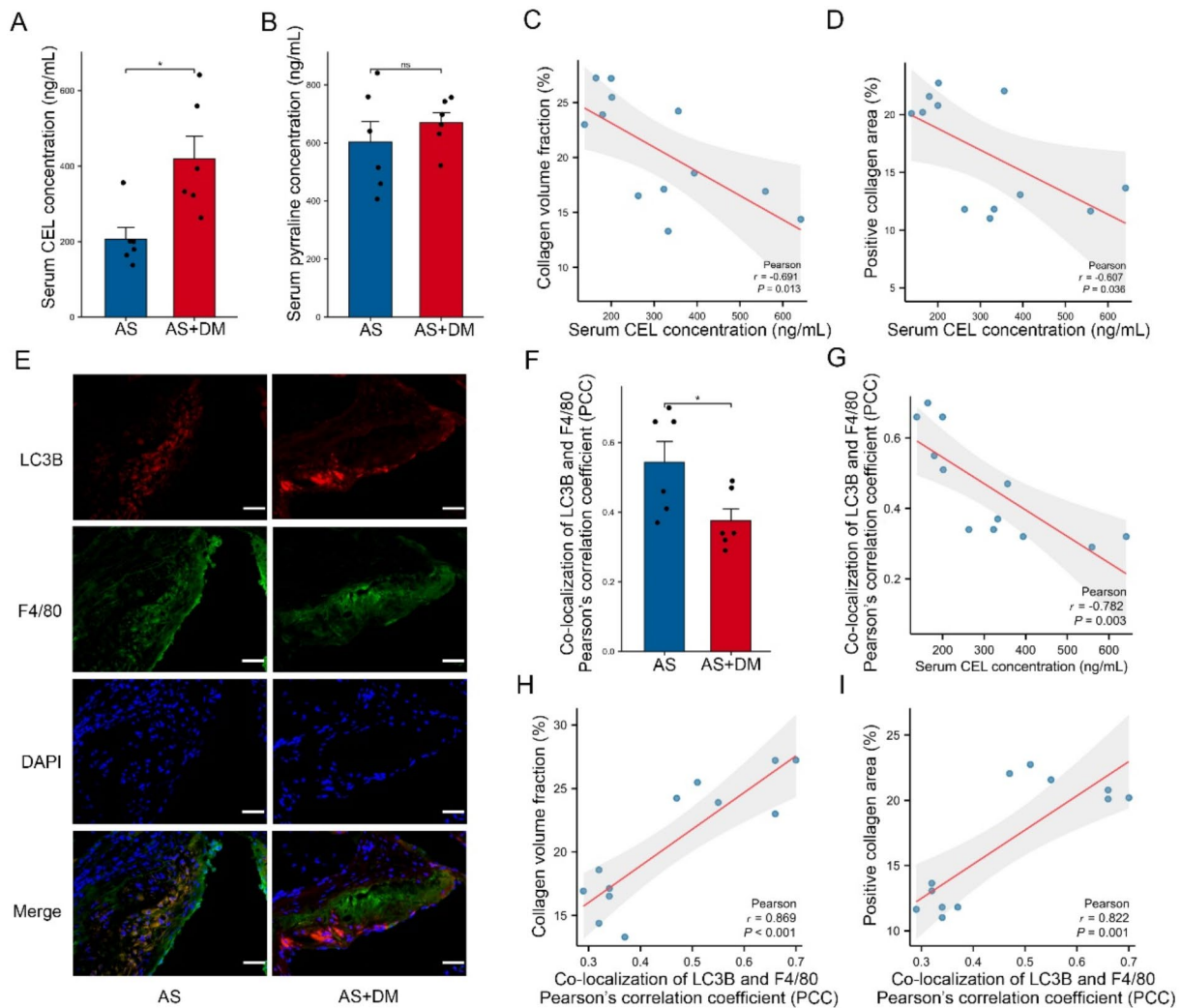


Fig. 3 Correlation of serum CEL concentrations with plaque vulnerability and macrophage autophagy in mice model. **A**, Serum carboxyethyl lysine (CEL) concentrations in atherosclerosis (AS) and diabetes-exacerbated atherosclerosis (AS+DM) mice. **B**, Serum pyrraline levels compared between AS and AS+DM mice. **C**, Scatter plot showing the negative correlation between serum CEL concentrations and collagen volume fraction as identified by Masson's trichrome staining; significant correlation noted ($r = -0.961$, $P = 0.013$). **D**, Positive correlation between serum CEL concentrations and the percentage of collagen-positive area, as detected by Sirius red staining ($r = 0.607$, $P = 0.036$). **E**, Representative double immunofluorescent stained images of aortic root plaques for LC3B and F4/80 with a scale bar of 100 μm . **F**, Quantitative analysis of the co-localization of LC3B and F4/80, assessed using Pearson's correlation coefficient (PCC). **G**, Scatter plot demonstrating the negative correlation between serum CEL concentration and PCC of LC3B-F4/80 co-localization ($r = -0.782$, $P = 0.003$). **H**, Positive correlation between PCC of LC3B-F4/80 co-localization and collagen volume fraction, identified by Masson's trichrome staining ($r = 0.869$, $P < 0.001$). **I**, Positive correlation shown between PCC of LC3B-F4/80 co-localization and the percentage of collagen-positive area, detected by Sirius red staining ($r = 0.869$, $P < 0.001$). Data are presented as mean \pm SD for $n = 6$ mice per group, with $*P < 0.05$ indicating statistical significance, and ns indicating non-significance ($P > 0.05$)

CEL exposure altered RAGE/LKB1/AMPK1/SIRT1 signaling in both mice primary macrophages and THP-1 cells

To establish a baseline understanding of the effects of CEL, SRT1720, and EX527 on SIRT1 activity, we conducted control experiments as shown in Figure S6. These experiments revealed that CEL significantly reduced SIRT1 activity, while SRT1720 enhanced it and EX527 inhibited it. These findings provided critical context for

interpreting the modulatory effects of these compounds in subsequent experiments. Figure 5A and Figure S7 demonstrate that CEL exposure induces a significant, concentration-dependent reduction in the NAD^+/NADH ratio in both mouse primary macrophages and THP-1 cells. The NAD^+/NADH ratio directly influences the activity of NAD^+ -dependent enzymes such as SIRT1. Measuring this ratio helps to evaluate whether CEL affects the

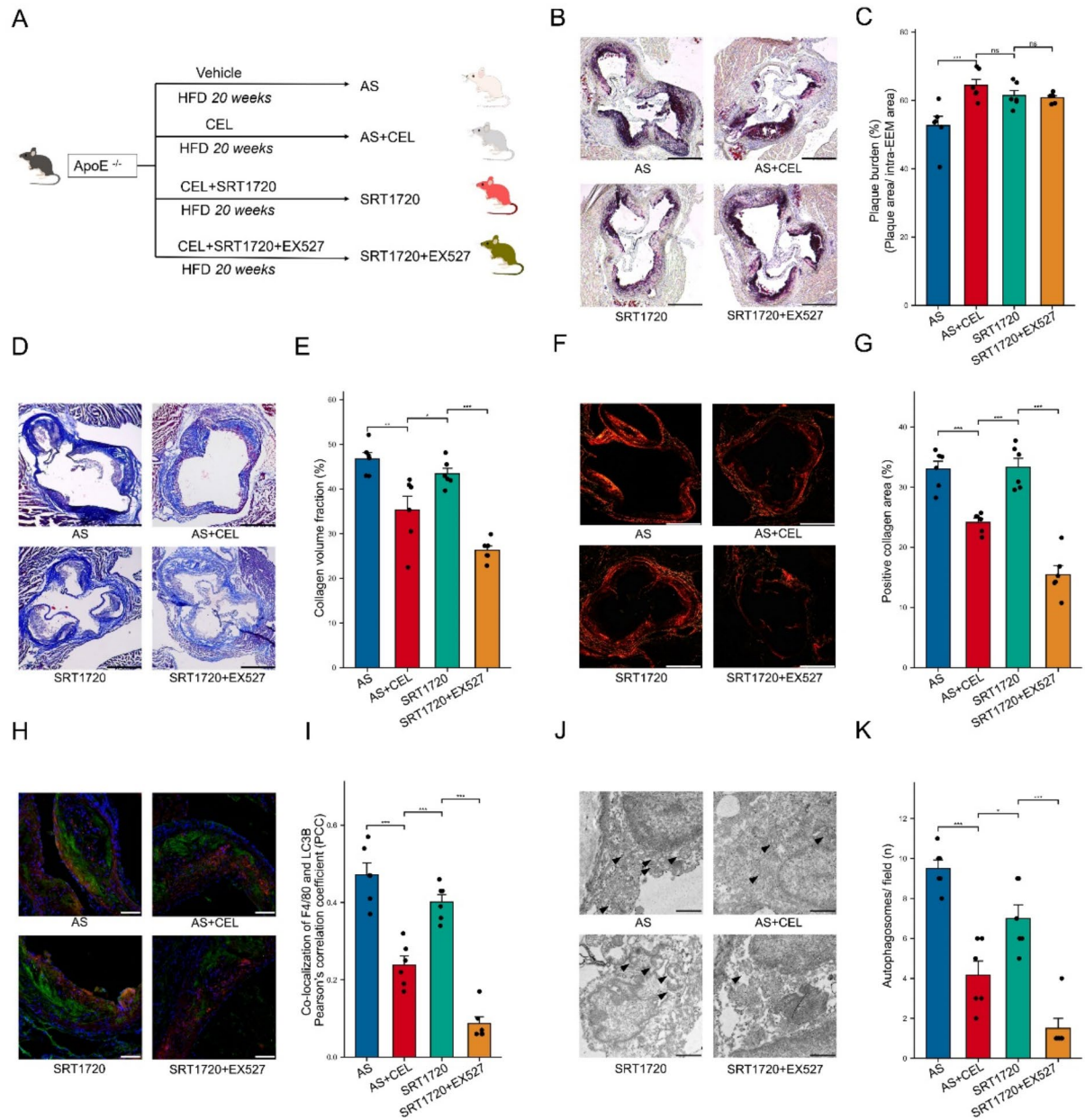


Fig. 4 Evaluating the impact of SIRT1 activity modulation on CEL-induced atherosclerotic plaque vulnerability and macrophage autophagy. **A**, Flowchart depicting the treatment and grouping of ApoE^{-/-} mice: mice were fed a high-fat diet (HFD) for 20 weeks to establish an atherosclerotic model (AS). Mice in the AS group treated with carboxyethyl lysine (CEL) were categorized as AS+CEL. Those in the AS+CEL group further treated with SRT1720 were designated as SRT1720, and mice in the SRT1720 group additionally treated with EX527 were categorized as SRT1720+EX527. **B**, Oil Red O (ORO) staining of aortic root plaques in AS, AS+CEL, SRT1720, and SRT1720+EX527 groups. **C**, Quantification of plaque area expressed as a ratio to the intra-external elastic membrane (EEM) area. Scale bars: 200 μ m. **D**, Representative images of aortic root plaques subjected to Masson's trichrome staining; scale bar: 200 μ m. **E**, Quantification of collagen volume fraction in plaques for each group. **F**, Representative images of aortic root plaques stained with Sirius red; scale bar: 200 μ m. **G**, Quantification of the positive collagen area in plaques across all groups. **H**, Representative double immunofluorescent stained images of aortic root plaques for LC3B and F4/80. Scale bar = 100 μ m. **I**, Quantitative analysis of the co-localization of LC3B and F4/80, assessed using Pearson's correlation coefficient (PCC). **J**, Representative transmission electron microscopy (TEM) images of plaque macrophages, highlighting autophagosomes (indicated by black arrows); scale bar = 1 μ m. **K**, Quantitative analysis of autophagy by comparing the number of autophagosomes per field in plaque macrophages among AS, AS+CEL, SRT1720, and SRT1720+EX527 groups. Data are presented as mean \pm SD for $n=6$ mice per group; significance denoted by *** $P < 0.001$, ** $P < 0.01$, * $P < 0.05$

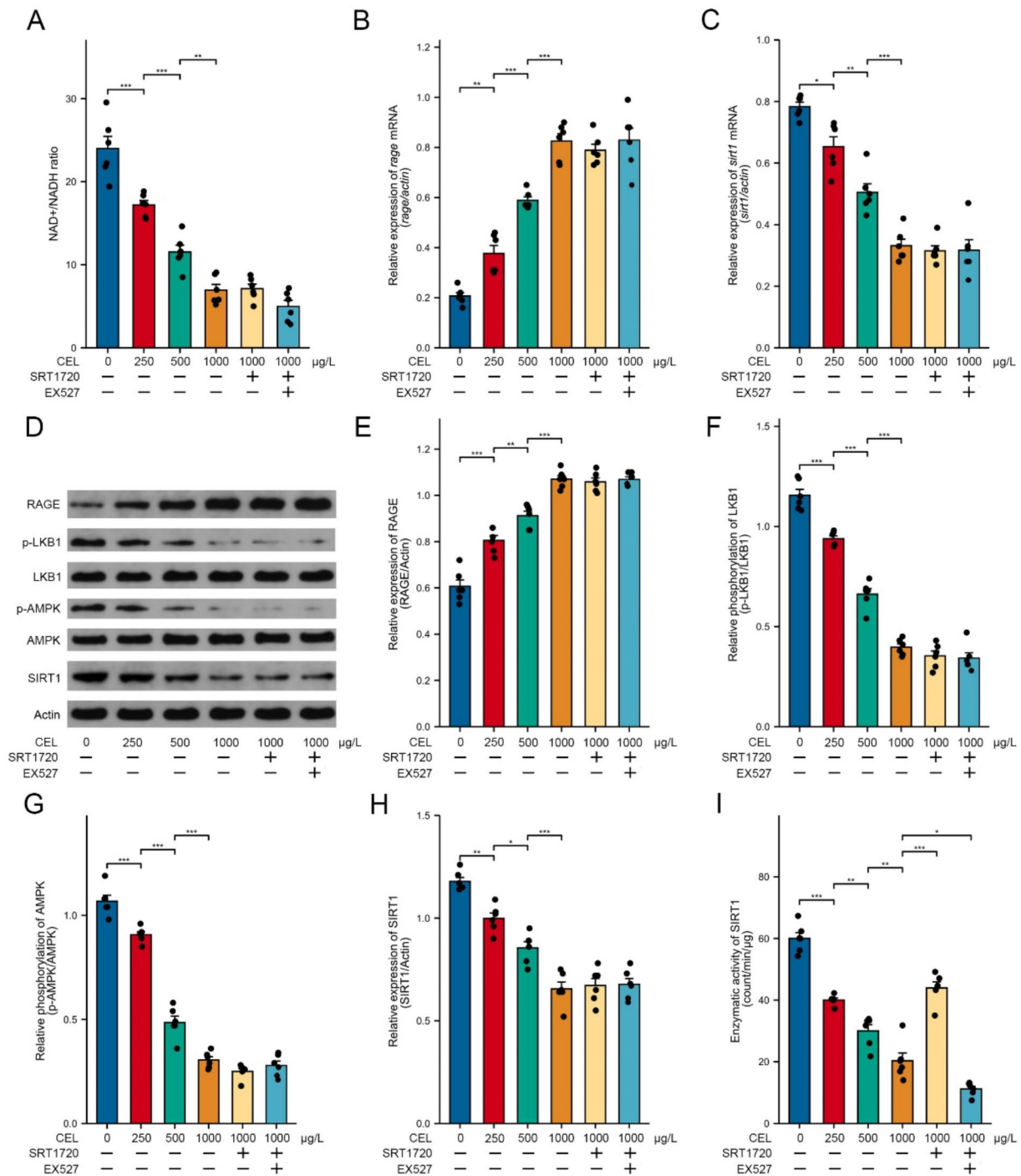


Fig. 5 Impact of SIRT1 activity modulation on CEL-induced RAGE/LKB1/AMPK/SIRT1 pathway in primary macrophages. **A**, Columnar representation of the NAD⁺/NADH ratio in primary macrophages treated with carboxethyl lysine (CEL) and co-treated with SRT1720 and/or EX527. **B**, Columns showing the relative expression levels of RAGE mRNA in macrophages subjected to the indicated treatments. **C**, Columns depicting the relative expression levels of SIRT1 mRNA in treated macrophages. **D**, Representative Western blots for RAGE, phosphorylated LKB1 (p-LKB1), total LKB1, phosphorylated AMPK (p-AMPK), total AMPK, SIRT1, and Actin in macrophages exposed to CEL, SRT1720, and/or EX527. **E**, Quantitative analysis of RAGE protein expression across different treatment groups. **F**, Columns indicating the relative phosphorylation levels of LKB1 in the macrophage samples. **G**, Columns showing the relative phosphorylation levels of AMPK under the various treatment conditions. **H**, Quantification of SIRT1 protein expression in treated macrophages. **I**, Enzymatic activity of SIRT1 detected in primary macrophages following exposure to CEL, with or without SRT1720/EX527 co-treatment. Data are presented as mean ± SD for n=6 independent replicates per experiment; statistical significance is indicated as *P < 0.05, **P < 0.01, ***P < 0.001

availability of NAD⁺, a crucial cofactor for SIRT1 activity. Notably, neither SRT1720 nor co-treatment with EX527 influenced the NAD⁺/NADH ratio in CEL-treated cells. As shown in Fig. 5B and C and Figure S7, CEL exposure markedly increased *rage* mRNA expression while concurrently decreasing *sirt1* mRNA expression in a dose-dependent manner. Neither SRT1720 nor co-treatment with EX527 significantly altered the mRNA expression levels of *rage* and *sirt1*. Protein analyses, depicted in Fig. 5D and H and Figure S7, revealed that CEL exposure substantially elevated RAGE protein levels while reducing the phosphorylation states of LKB1 and AMPK, as well as the overall expression of SIRT1, in a concentration-dependent manner. Similarly, neither SRT1720 nor co-treatment with EX527 influenced the expression or phosphorylation levels of these proteins. Finally, Fig. 5I and Figure S7 show that CEL exposure led to a pronounced, dose-dependent reduction in SIRT1 catalytic activity. While SRT1720 effectively preserved SIRT1 catalytic activity in CEL-treated cells, this effect was impaired by co-treatment with EX527. To further validate the role of RAGE, LKB1, and AMPK1 in mediating the effects of CEL on SIRT1 activity, we employed genetic manipulation strategies. Specifically, siRNA-mediated silencing of RAGE significantly attenuated CEL-induced inhibition of SIRT1 catalytic activity. Similarly, overexpression of LKB1 or AMPK1 using plasmids mitigated the inhibitory effects of CEL on SIRT1 activity. These results, presented in Figure S8, provide strong evidence that CEL exerts its effects on SIRT1 through the RAGE/LKB1/AMPK1 signaling pathway.

CEL exposure modulated macrophage autophagy via SIRT1-dependent ZKSCAN3 acetylation

In our studies, Fig. 6A–B and Figure S9 illustrate that exposure to CEL decreases the nuclear translocation of ZKSCAN3 compared to controls, while subsequent higher concentrations of CEL enhance ZKSCAN3's nuclear localization in a concentration-dependent manner. This nuclear localization of ZKSCAN3 plays a critical role in repressing autophagic gene expression, including MAP1LC3B. CEL exposure modulates this process through SIRT1-dependent acetylation: lower concentrations reduce ZKSCAN3 acetylation and nuclear localization, potentially relieving repression on autophagic genes, while higher concentrations increase ZKSCAN3 acetylation, promoting its nuclear localization and suppressing autophagic activity. Notably, SRT1720 administration significantly reduces, and EX527 co-treatment further impairs, this nuclear translocation. Co-immunoprecipitation (Co-IP) analyses (Fig. 6C and E) reveal that CEL exposure initially reduces ZKSCAN3 acetylation levels, whereas increasing CEL concentrations elevate these levels; however, SRT1720 markedly decreases, and

EX527 co-treatment significantly increases ZKSCAN3 acetylation. Chromatin immunoprecipitation (ChIP) assays (Fig. 6F and G) demonstrate that CEL exposure diminishes, and higher concentrations of CEL enhance, ZKSCAN3's binding affinity to the *map1lc3b* promoter, with SRT1720 weakening and EX527 co-treatment intensifying this interaction. Furthermore, evaluation of the autophagic response through the LC3II expression and autophagic flux (Fig. 6H and L) indicates that CEL exposure stimulates autophagy compared to controls, but higher concentrations of CEL impair autophagy in a concentration-dependent manner in primary macrophages. Remarkably, while SRT1720 alleviates this inhibition, EX527 exacerbates it in CEL-exposed macrophages. Similar results were observed in human THP-1 cells (Figure S10).

Discussion

Atherosclerosis, a chronic inflammatory disease marked by the accumulation of lipids and fibrous elements in the arteries, significantly worsens under T2DM, heightening cardiovascular risks significantly [22]. The interplay between diabetes-induced metabolic disorders and atherosclerosis escalates not only the complexity of the disease but also the severity of potential cardiovascular events [23]. This study delved into this interplay by examining the impact of CEL, a typical AGEs, on the stability of atherosclerotic plaques and macrophage autophagy, offering insights into the pathological contributions of AGEs in diabetic atherosclerosis.

Our findings indicated that diabetic conditions (AS+DM group) exacerbate plaque instability compared to non-diabetic conditions (AS group). This was evidenced by increased plaque burden and decreased collagen content, which are critical indicators of plaque vulnerability to rupture [24]. The degradation of collagen, essential for maintaining the structural integrity of the arterial wall, points towards the increased fragility of blood vessels typically observed in diabetic patients [25, 26]. Elevated levels of CEL in individuals with T2DM were closely correlated with the incidence of acute coronary syndrome (ACS) [27]. This association underscores the critical impact of glycation products like CEL in promoting endothelial dysfunction and inflammatory responses, which contribute to the progressive destabilization of atherosclerotic plaques.

The inverse relationship between serum CEL concentrations and plaque collagen content suggests that increased CEL levels may contribute to reduced plaque stability. Interestingly, initial exposure to lower concentrations of CEL appeared to stimulate macrophage autophagic activity compared to controls, which may serve as a protective mechanism against cellular stress. However, as CEL concentrations increase, the initial

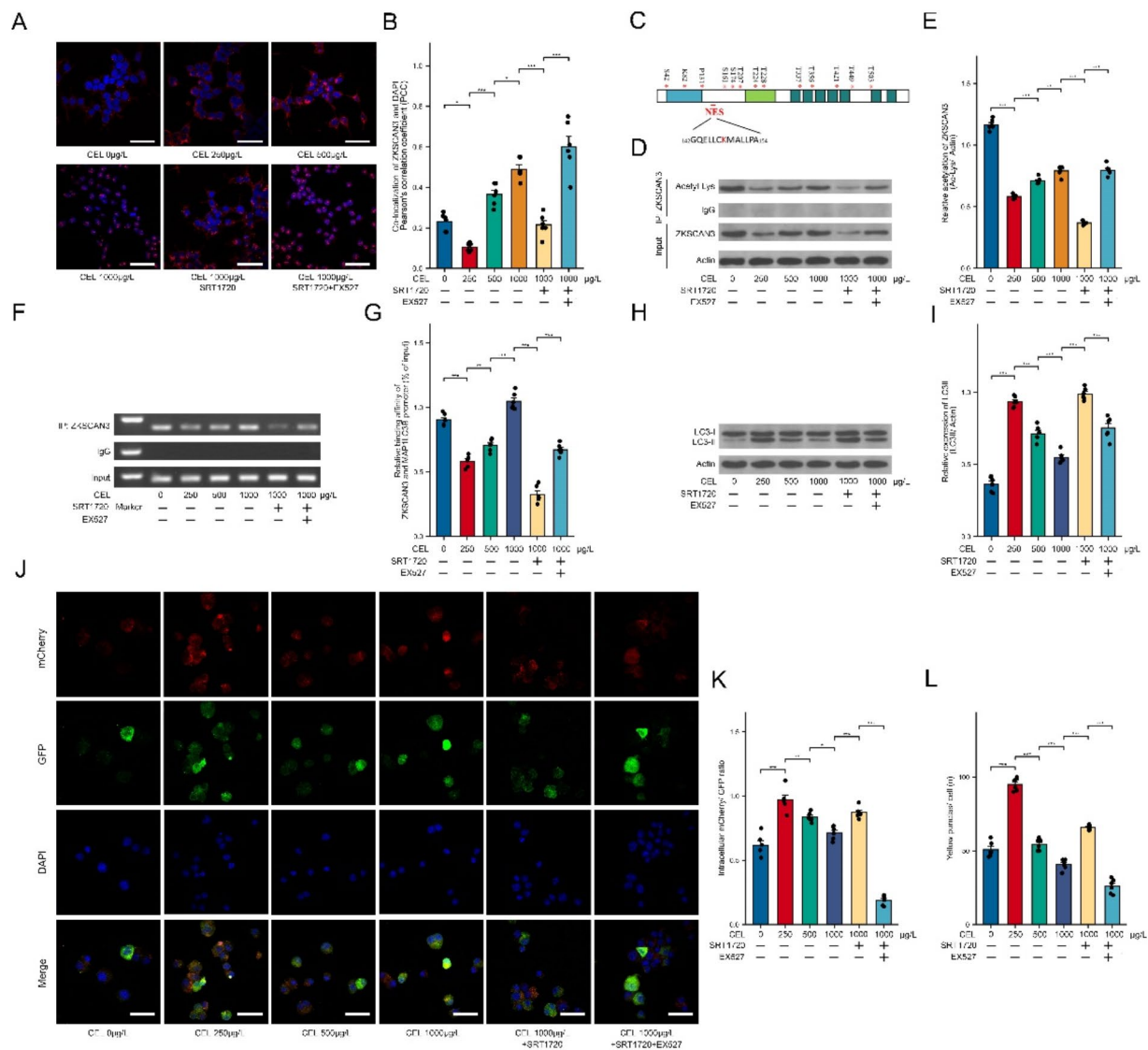


Fig. 6 Evaluation of SIRT1 activity modulation on ZKSCAN3-regulated autophagy in CEL-treated macrophages. **A**, Representative merged images of ZKSCAN3 immunofluorescence staining counterstained with DAPI in primary macrophages treated with CEL and co-treated with SRT1720 and/or EX527; scale bar = 50 μm. **B**, Quantification of ZKSCAN3 and DAPI co-localization using Pearson's correlation coefficient (PCC) in treated macrophages. **C**, Prediction of potential SIRT1 lysine residues; Lys148 located within the nuclear export signal (NES) region. **D**, Co-immunoprecipitation assays were used to assess ZKSCAN3 acetylation levels in macrophages under various treatment conditions. **E**, Relative acetylation levels of ZKSCAN3 as influenced by CEL and co-treatments. **F**, Chromatin immunoprecipitation (ChIP) assays evaluating the binding affinity of ZKSCAN3 to the *map1lc3b* promoter. **G**, Quantitative analysis of the relative binding affinity of ZKSCAN3 to the *map1lc3b* promoter in macrophages treated as specified. **H**, Western blot analysis of LC3 protein expression to assess autophagy. **I**, Relative expression levels of LC3II in the treated macrophage groups. **J**, Ad-mCherry-GFP-LC3B recombinant adenovirus transfection for autophagy detection; representative images of mCherry, GFP, DAPI, and their merged visualization are displayed. **K**, Autophagy quantification through intracellular mCherry/GFP ratio. **L**, Average number of yellow puncta per cell indicating autophagic vesicles in treated macrophages. Data are presented as mean ± SD for *n* = 6 independent replicates per experiment; significance indicated by **P* < 0.05, ***P* < 0.01, ****P* < 0.001.

autophagic activation transitions into inhibition, highlighting a concentration-dependent biphasic effect on this cellular process. While the inhibition of autophagy at higher concentrations does not reach levels lower than the control condition, the observed trend still suggests a reduction in autophagic activity relative to the

lower concentrations, indicating that CEL may modulate autophagy in a dose-dependent manner.

We hypothesize that at lower concentrations, CEL might promote autophagy as an adaptive response to stress, whereas at higher concentrations, CEL's inhibition of SIRT1 activity leads to a suppression of autophagy. This shift from autophagy promotion to inhibition

is likely driven by the increasing SIRT1 inhibition as CEL concentration rises, which overwhelms the initial autophagic activation. The SIRT1-dependent mechanism explains this biphasic response, where low levels of CEL may initiate protective autophagic activity, but high levels of CEL ultimately suppress autophagy as SIRT1's inhibitory effect becomes dominant. The ability of pharmacological agents, such as SIRT1 activators (e.g., SIRT1720), to restore autophagy levels even in the presence of CEL underscores the therapeutic potential of targeting the SIRT1-dependent pathway.

The diminished macrophage autophagic activity observed in the AS+DM group, in conjunction with the negative correlation between serum CEL levels and macrophage autophagic activity, points to a potential regulatory role of CEL in macrophage autophagy within atherosclerotic plaques. We interpret this finding with the understanding that at higher concentrations, CEL suppresses autophagy through SIRT1 inhibition, which is more pronounced at elevated CEL levels, leading to the reduction of autophagic activity. Given that macrophage autophagy is crucial for maintaining plaque stability [28], the findings suggest that abnormal accumulation of CEL in T2DM conditions might exacerbate atherosclerosis by impairing macrophage autophagy and subsequently compromising plaque stability.

RAGE, as a receptor for AGEs, has been previously implicated in various pathophysiological processes, including inflammation and oxidative stress, both of which can influence autophagy [29]. A previous investigation suggested that the V domain of RAGE made molecular contacts with CEL moiety and the peptide backbone in the immediate vicinity of CEL, providing specific and stable binding which further activate RAGE signaling [13]. Once activated, RAGE can influence the LKB1/AMPK axis, a central regulator of cellular energy homeostasis [30]. LKB1 acts as an upstream kinase for AMPK1, and any perturbation in its activity can directly impact AMPK1's role in maintaining cellular energy balance and promoting autophagy under stress conditions [31]. SIRT1, a NAD⁺-dependent deacetylase, is another crucial player in this pathway. AMPK1 can enhance the activity of SIRT1 by increasing cellular NAD⁺ levels. The observed downregulation of SIRT1 in the presence of elevated CEL levels leading to impaired SIRT1-dependent autophagy. Our experiments using RAGE silencing (siRNA) further demonstrated that CEL's effects on autophagy and SIRT1 activity are mediated, at least in part, through RAGE signaling. Silencing RAGE significantly alleviated the CEL-induced suppression of SIRT1 activity and autophagy, supporting the critical role of RAGE in this pathological process. These findings suggest that targeting RAGE could provide a novel

therapeutic approach to mitigating plaque instability in diabetic atherosclerosis.

ZKSCAN3, a zinc-finger transcriptional repressor, has been previously implicated in the negative regulation of autophagy [32]. Its nuclear localization suppresses autophagic gene expression, while its cytoplasmic retention relieves this repression. CEL exposure modulates ZKSCAN3 nuclear localization in a dose-dependent manner through SIRT1-dependent acetylation. Our findings suggest that CEL exposure promotes the nuclear localization of ZKSCAN3, potentially suppressing autophagic gene MAP1LC3B expression. The pivotal role of SIRT1, a NAD⁺-dependent deacetylase, in this process is evident from its ability to deacetylate ZKSCAN3, thereby modulating its nuclear translocation [33]. The observed increase in ZKSCAN3 acetylation upon CEL exposure, coupled with its reduced or increased acetylation following SIRT1720 or EX527 treatment, underscores the significance of SIRT1 in this regulatory cascade. Furthermore, the enhanced binding affinity of ZKSCAN3 to the MAP1LC3B promoter in the presence of CEL suggests a direct transcriptional repression of autophagy-related genes. SIRT1 plays a central role in this biphasic response. In the presence of lower CEL concentrations, SIRT1 suppression is less pronounced, allowing autophagy to be activated via other pathways, leading to a protective autophagic response. However, as the CEL concentration increases, the suppression of SIRT1 becomes more pronounced. This stronger inhibition of SIRT1 leads to a reversal of the autophagic response, causing the process to shift from activation to inhibition. At higher concentrations of CEL, SIRT1 suppression becomes the dominant mechanism, leading to autophagic inhibition.

Our study highlights the biphasic effects of CEL, which appear to stem from its dose-dependent modulation of distinct signaling pathways. At lower concentrations, CEL may enhance protective mechanisms such as SIRT1 activation, promoting metabolic homeostasis and cell survival. This effect is likely mediated through the activation of LKB1/AMPK1 signaling and the suppression of RAGE-driven oxidative stress, as supported by studies linking SIRT1 to improved cellular resilience [34]. Conversely, at higher concentrations, CEL induces stress responses, characterized by increased RAGE activation and impaired phosphorylation of LKB1 and AMPK1, leading to the inhibition of SIRT1 activity and subsequent cellular dysfunction. This dual action aligns with the concept of hormesis, where compounds exert opposing effects depending on dose [35]. The observed biphasic effects also suggest potential secondary targets of CEL at higher concentrations, which could exacerbate oxidative stress or autophagic dysregulation. Autophagy modulation has been implicated in similar biphasic phenomena,

where low-level activation is cytoprotective, but excessive activation leads to autophagic cell death [36].

In summary, our study elucidates the mechanisms by which CEL affects plaque stability through regulating macrophage autophagy in T2DM via modulating the RAGE/LKB1/AMPK1/SIRT1 pathway and SIRT1-dependent ZKSCAN3 acetylation. The evidence from RAGE silencing experiments further emphasizes RAGE's role as a central mediator in this pathway. These findings suggest that targeting the RAGE/SIRT1 axis could mitigate plaque instability in diabetic atherosclerosis, providing a basis for developing novel therapeutic strategies. Further clinical studies are warranted to validate these therapeutic potentials.

Limitations and perspectives

While our study provides valuable insights into the role of CEL in plaque stability and macrophage autophagy, there are inherent limitations. The murine model, though widely accepted, may not fully replicate the complexities of human T2DM and its cardiovascular implications. Additionally, the study primarily focused on specific signaling pathways, potentially overlooking other concurrent mechanisms influenced by CEL. While we observed dose-dependent biphasic effects of CEL *in vitro*, the precise molecular mechanisms remain unclear, particularly at higher concentrations where secondary targets may play a role. Future research should consider a broader spectrum of molecular interactions and employ diverse models, including human samples, to validate and expand upon our findings. The therapeutic potential of targeting these pathways in clinical settings remains an exciting avenue for exploration.

Supplementary Information

The online version contains supplementary material available at <https://doi.org/10.1186/s12933-025-02586-y>.

Supplementary Material 1.

Author contributions

Z.L. and J.L. conceptualized the study. Y.Z., Y.M., and G.G. conducted the investigations. Y.Y., N.H., and X.L. curated the data. X.W., X.Y., and S.M. performed the formal analysis. J.W. and J.Z. supervised the project. Z.L. and X.W. acquired funding. Z.L. and J.W. drafted the original manuscript. J.Z., L.Z., and Y.Z. provided critical revisions. All authors reviewed the manuscript.

Funding

This study was generously supported by multiple grants: the National Natural Science Foundation of China (Grant No. 82070858) awarded to Z.L.; the Youth Scientific Research and Innovation Team Program of Shaanxi Province (Grant No. 2022-SLRH-LJ-014) to Z.L.; the QinChuangYuan TCM Innovation and Research Project (Grant No. 2022-QCYZH-016) to Z.L.; the Traditional Chinese Medicine Research Innovation Talent Program (TZKN-CXRC-15) to Z.L.; the Basic Scientific Research Operating Expenses from Xi'an Jiaotong University (Grant No. xzy012022131) to X.W.; the China Postdoctoral Science Foundation (Grant No. 2022M722576) to W.X.; the Shaanxi Provincial Postdoctoral Foundation (First-class support, Grant No. 127) to X.W.; the Xi'an Innovation Ability Support Plan (Grant No. 23YXYJ0187) to X.W.

Data availability

No datasets were generated or analysed during the current study.

Declarations

Competing interests

The authors declare no competing interests.

Author details

¹Department of Cardiology, Shaanxi Provincial People's Hospital, 256 Youyi Xi Rd, Xi'an 710068, China

²Atherosclerosis Integrated Chinese and Western Medicine Key Research Laboratory, Research Office of Shaanxi Administration of Traditional Chinese Medicine, Xi'an 710003, China

³Department of Technology Transfer and Management, Shaanxi Provincial People's Hospital, Xi'an 710068, China

⁴Affiliated Shaanxi Provincial People's Hospital, Northwestern Polytechnical University, Xi'an 710068, China

⁵School of Medicine, Xizangminzu University, Xianyang 712082, China

⁶School of Medicine, Yan'an University, Yan'an 716000, China

⁷Traditional Chinese Medicine Inheritance and Innovation Platform, Shaanxi Provincial People's Hospital, Xi'an 710068, China

⁸Department of Nursing, Shaanxi Provincial People's Hospital, Xi'an 710068, China

⁹Department of Otolaryngology, Shaanxi Provincial People's Hospital, 256 Youyi Xi Rd, Xi'an 710068, China

¹⁰The Director's Office, Shaanxi Provincial People's Hospital, 256 Youyi Xi Rd, Xi'an 710068, China

Received: 31 July 2024 / Accepted: 7 January 2025

Published online: 22 January 2025

References

1. Libby P. The changing landscape of atherosclerosis. *Nature*. 2021;592(7855):524–33.
2. Viigimaa M, Sachinidis A, Toumpourleka M, Koutsampasopoulos K, Alliksoo S, Titma T. Macrovascular complications of type 2 diabetes mellitus. *Curr Vasc Pharmacol*. 2020;18(2):110–6.
3. Yun JS, Ko SH. Current trends in epidemiology of cardiovascular disease and cardiovascular risk management in type 2 diabetes. *Metabol Clin Exp*. 2021;123:154838.
4. Bonora E, Kiechl S, Oberhollenzer F, Egger G, Bonadonna RC, Muggeo M, Willeit J. Impaired glucose tolerance, type II diabetes mellitus and carotid atherosclerosis: prospective results from the Bruneck Study. *Diabetologia*. 2000;43(2):156–64.
5. Yurdagul A Jr. Crosstalk between macrophages and vascular smooth muscle cells in atherosclerotic plaque stability. *Arterioscler Thromb Vasc Biol*. 2022;42(4):372–80.
6. Tabas I, Bornfeldt KE. Macrophage phenotype and function in different stages of atherosclerosis. *Circ Res*. 2016;118(4):653–67.
7. Schrijvers DM, De Meyer GR, Herman AG, Martinet W. Phagocytosis in atherosclerosis: molecular mechanisms and implications for plaque progression and stability. *Cardiovasc Res*. 2007;73(3):470–80.
8. Khalid M, Petroianu G, Adem A. Advanced glycation end products and diabetes mellitus: mechanisms and perspectives. *Biomolecules* 2022, 12(4).
9. Fukami K, Yamagishi S, Okuda S. Role of AGEs-RAGE system in cardiovascular disease. *Curr Pharm Des*. 2014;20(14):2395–402.
10. Barlovic DP, Soro-Paavonen A, Jandeleit-Dahm KA. RAGE biology, atherosclerosis and diabetes. *Clin Sci*. 2011;121(2):43–55.
11. Yuan T, Yang T, Chen H, Fu D, Hu Y, Wang J, Yuan Q, Yu H, Xu W, Xie X. New insights into oxidative stress and inflammation during diabetes mellitus-accelerated atherosclerosis. *Redox Biol*. 2019;20:247–60.
12. Wang Z, Yan J, Li L, Liu N, Liang Y, Yuan W, Chen X. Effects of Nε-carboxymethyl-Lysine on ERS-mediated apoptosis in diabetic atherosclerosis. *Int J Cardiol*. 2014;172(3):e478–483.
13. Xue J, Rai V, Singer D, Chabierski S, Xie J, Reverdatto S, Burz DS, Schmidt AM, Hoffmann R, Shekhtman A. Advanced glycation end product recognition by the receptor for AGEs. *Struct (London England: 1993)*. 2011;19(5):722–32.

14. Ajith TA, Vinodkumar P. Advanced glycation end products: association with the pathogenesis of diseases and the current therapeutic advances. *Curr Clin Pharmacol*. 2016;11(2):118–27.
15. Liang B, Zhou Z, Yang Z, Liu J, Zhang L, He J, Li H, Huang Y, Yang Q, Xian S, et al. AGEs-RAGE axis mediates myocardial fibrosis via activation of cardiac fibroblasts induced by autophagy in heart failure. *Exp Physiol*. 2022;107(8):879–91.
16. Byrne RA, Rossello X, Coughlan JJ, Barbato E, Berry C, Chieffo A, Claeys MJ, Dan GA, Dweck MR, Galbraith M, et al. 2023 ESC guidelines for the management of acute coronary syndromes. *Eur Heart J*. 2023;44(38):3720–826.
17. ElSayed NA, Aleppo G, Aroda VR, Bannuru RR, Brown FM, Bruemmer D, Collins BS, Hilliard ME, Isaacs D, Johnson EL, et al. 2. Classification and diagnosis of diabetes: standards of care in diabetes-2023. *Diabetes Care*. 2023;46(Suppl 1):S19–40.
18. Kim TH, Young SL, Sasaki T, Deaton JL, Schammel DP, Palomino WA, Jeong JW, Lessey BA. Role of sirt1 and progesterone resistance in normal and abnormal endometrium. *J Clin Endocrinol Metabol*. 2022;107(3):788–800.
19. Zhong Y, Liao J, Hu Y, Wang Y, Sun C, Zhang C, Wang G. PM(2.5) upregulates MicroRNA-146a-3p and induces M1 polarization in RAW264.7 cells by targeting sirtuin1. *Int J Med Sci*. 2019;16(3):384–93.
20. Munk SHN, Merchut-Maya JM, Adelantado Rubio A, Hall A, Pappas G, Milletti G, Lee M, Johnsen LG, Guldborg P, Bartek J, et al. NAD(+) regulates nucleotide metabolism and genomic DNA replication. *Nat Cell Biol*. 2023;25(12):1774–86.
21. Li RL, Lu ZY, Huang JJ, Qi J, Hu A, Su ZX, Zhang L, Li Y, Shi YQ, Hao CN, et al. SRT1720, a SIRT1 specific activator, protected H2O2-induced senescent endothelium. *Am J Transl Res*. 2016;8(7):2876–88.
22. Libby P, Buring JE, Badimon L, Hansson GK, Deanfield J, Bittencourt MS, Tokgözoğlu L, Lewis EF. Atherosclerosis. *Nat Rev Disease Primers*. 2019;5(1):56.
23. Bornfeldt KE, Tabas I. Insulin resistance, hyperglycemia, and atherosclerosis. *Cell Metabol*. 2011;14(5):575–85.
24. Moreno PR, Murcia AM, Palacios IF, Leon MN, Bernardi VH, Fuster V, Fallon JT. Coronary composition and macrophage infiltration in atherectomy specimens from patients with diabetes mellitus. *Circulation*. 2000;102(18):2180–4.
25. Virmani R, Kolodgie FD, Burke AP, Farb A, Schwartz SM. Lessons from sudden coronary death: a comprehensive morphological classification scheme for atherosclerotic lesions. *Arterioscler Thromb Vasc Biol*. 2000;20(5):1262–75.
26. Finn AV, Nakano M, Narula J, Kolodgie FD, Virmani R. Concept of vulnerable/unstable plaque. *Arterioscler Thromb Vasc Biol*. 2010;30(7):1282–92.
27. Yan SF, Ramasamy R, Schmidt AM. Mechanisms of disease: advanced glycation end-products and their receptor in inflammation and diabetes complications. *Nat Clin Pract Endocrinol Metabol*. 2008;4(5):285–93.
28. Razani B, Feng C, Coleman T, Emanuel R, Wen H, Hwang S, Ting JP, Virgin HW, Kastan MB, Semenkovich CF. Autophagy links inflammasomes to atherosclerotic progression. *Cell Metabol*. 2012;15(4):534–44.
29. Kang R, Tang D, Lotze MT, Zeh HJ. 3rd: RAGE regulates autophagy and apoptosis following oxidative injury. *Autophagy*. 2011;7(4):442–4.
30. Yu W, Liu-Bryan R, Stevens S, Damanahalli JK, Terkeltaub R. RAGE signaling mediates post-injury arterial neointima formation by suppression of liver kinase B1 and AMPK activity. *Atherosclerosis*. 2012;222(2):417–25.
31. Kottakis F, Bardeesy N. LKB1-AMPK axis revisited. *Cell Res*. 2012;22(12):1617–20.
32. Pan H, Yan Y, Liu C, Finkel T. The role of ZKSCAN3 in the transcriptional regulation of autophagy. *Autophagy*. 2017;13(7):1235–8.
33. Wu X, Ren Y, Wen Y, Lu S, Li H, Yu H, Li W, Zou F. Deacetylation of ZKSCAN3 by SIRT1 induces autophagy and protects SN4741 cells against MPP(+)-induced oxidative stress. *Free Radic Biol Med*. 2022;181:82–97.
34. Singh V, Ubaid S. Role of silent information regulator 1 (SIRT1) in regulating oxidative stress and inflammation. *Inflammation*. 2020;43(5):1589–98.
35. Oberbaum M, Cambar J. Hormesis: Dose-Dependent Reverse Effects of Low and Very Low Doses. In: *Ultra High Dilution: Physiology and Physics*. Edited by Endler PC, Schulte J. Dordrecht: Springer Netherlands; 1994: 5–18.
36. Levine B, Kroemer G. Autophagy in the pathogenesis of disease. *Cell*. 2008;132(1):27–42.

Publisher's note

Springer Nature remains neutral with regard to jurisdictional claims in published maps and institutional affiliations.